#### **Research Article**

MD. Shamshuddin, L. J. Sademaki, Subhajit Panda, S. R. Mishra, Umair Khan\*, and Basma Souayeh

# Central composite design modeling in optimizing heat transfer rate in the dissipative and reactive dynamics of viscoplastic nanomaterials deploying Joule and heat generation aspects

https://doi.org/10.1515/ntrev-2025-0228 received April 8, 2025; accepted September 27, 2025

**Abstract:** The objective of the proposed study is to investigate the magnetohydrodynamic flow characteristics of a Casson nanofluid transport on a nonlinear oblique extending absorbent surface, considering the role of heat generation and Ohmic heating. The incorporation of Ohmic heating in a viscoplastic nanofluid plays a crucial role in enhancing the uniqueness of this work. This Ohmic heating significantly affects heat transport properties and nanofluid flow behavior in more effective energy transfer frameworks. Also, the Buongiorno model is a widely used and precise technique for the modeling of fluid flow problems utilized in solar systems. Similarity conversions are utilized to minimize the leading equations into a set of coupled ordinary differential

equations (ODEs) from controlling partial differential equations. These coupled ODEs governing the momentum, heat, and mass are numerically solved. The Runge-Kutta fourth order method combined with the shooting technique for the non-dimensional governing ODEs is employed to analyze the features of key aspects incorporated in the flow regime. A comprehensive scrutiny of controlling parameters is carried out, and numerical outcomes are depicted as graphical illustrations and in tabular format. In addition to this, the practical applications of engineering quantities on the Nusselt number are visualized and discussed via statistical analysis. The obtained outcomes are compared with results that have already been published, and a good match is found. The improvement of the Hartmann number, mass Grashof number (Gr), Casson parameter, and inclination angle reduces the fluid velocity, while increasing the thermal Gr exhibits an opposite behavior. Augmenting the thermal radiation parameter, Eckert number, thermophoresis, and Brownian motion parameter (Nb) enhances the fluid temperature distribution. The fluid temperature rises upon accelerating the thermophoresis parameter, while the contrary result is obtained upon improving the Lewis number and Nb. The drag friction coefficient is improved by enhancing the thermal Gr and Casson parameter.

**Keywords:** Casson nanofluid, two-phase model, Ohmic heating, heat generation, chemical reaction, oblique extending sheet

\* Corresponding author: Umair Khan, Department of Mathematics, Saveetha School of Engineering, Saveetha Institute of Medical and Technical Sciences, Saveetha University, Chennai, Tamil Nadu, 602105, India; Department of Mathematics, Faculty of Science, Sakarya University, Serdivan/Sakarya, 54050, Turkey, e-mail: umairkhan@sakarya.edu.tr

MD. Shamshuddin: Department of Mathematics, School of Computer Science and Artificial Intelligence, SR University, Warangal, Telangana, 506371, India, e-mail: shammaths@gmail.com, md.shamshuddin@sru.edu.in L. J. Sademaki: Department of Applied Science and Social Studies, Arusha Technical College, P.O. Box 296, Arusha, Tanzania, e-mail: jlsademaki@gmail.com

**Subhajit Panda:** Centre for Data Science, Department of Computer Science and Engineering, Siksha 'O' Anusandhan Deemed to be University, Bhubaneswar, Odisha, 751030, India, e-mail: spanda.math@gmail.com

**S. R. Mishra:** Department of Mathematics, Siksha 'O' Anusandhan Deemed to be University, Bhubaneswar, Odisha, 751030, India, e-mail: satyaranjan\_mshr@yahoo.co.in

Basma Souayeh: Department of Physics, King Faisal University, PO Box 400, Al-Ahsa, 31982, Saudi Arabia, e-mail: bsouayeh@kfu.edu.sa ORCID: MD. Shamshuddin 0000-0002-2453-8492; L. J. Sademaki 0000-0003-1357-7346; Subhajit Panda 0000-0002-4865-0657; S. R. Mishra 0000-0002-3018-394X

## Nomenclature

u, v velocity components (m s<sup>-1</sup>)

x, y Cartesian coordinates (m)

*α* Casson parameter

Ha magnetic parameter

Gm solutal buoyancy

Gr thermal Grashof number

Nr radiation parameter

Pr Prandtl number

2 — MD. Shamshuddin et al. DE GRUYTER

Nt	thermophoresis parameter
Nb	Brownian motion parameter
$J_{ m H}$	Joule heating parameter
$Q_0$	heat source parameter
Ec	Eckert number
Pr	Prandtl number
Le	Lewis number
Kc	chemical reaction parameter
S	suction parameter
$q_{ m w}$	heat flux
$q_{\mathrm{m}}$	mass flux
$D_{\mathrm{T}}$	thermal diffusion
$D_{ m B}$	Brownian diffusion
$Re_x$	local Reynolds number
$q_{ m r}$	radiative heat flux (kg s <sup>-3</sup> )
γ	thermal diffusivity
$\sigma^{\scriptscriptstyle  ext{S}}$	Stefan–Boltzmann constant (W m <sup>-2</sup> K <sup>-4</sup> )
$A_{\rm c}$	mean absorption coefficient (m <sup>-1</sup> )
T	temperature (K)
$T_{\infty}$	ambient temperature (K)
$\mu_{ ext{B}}$	dynamic viscosity (kg m <sup>-1</sup> s <sup>-1</sup> )

# 1 Introduction

 $c_{\rm p}$ 

specific heat capacity

electrical conductivity

Due to practical significance in the investigation of combined thermal and solutal transport in hydro-magnetic incompressible fluid across extending/dwindling sheets, numerous researchers have been attracted to investigating the flows through stretching and shrinking sheets. These kinds of flows find applications in the broad context of science and technology, including polymer processing, blood flow problems, glass fiber manufacturing, paper and condensation processes, hot rolling, cooling, etc. The boundary layer flow in elongating sheet investigations was pioneered by Sakiadis [1] who considered the continuous cylindrical surface. Later, Crane [2] scrutinized the fluid transport over a propelling elongating plate. Mabood performed a heat transmission analysis on the hydromagnetic boundary layer nanofluid transport past a nonlinear widening surface, where the flow solutions were obtained numerically. Rama Devi and Reddy [3] discussed the radiative and reactive efforts on hydro-magnetic nanofluid movement via an extending sheet. Consequently, studies of Rama Devi and Reddy, Khan et al., Sadighi et al., and Adel et al. [4-7] present fascinating findings that showcase the distinct behavior of various physical flow parameters of nanofluids past extending surfaces.

The effects of Ohmic heating and energy dissipation are highly critical in domains of large current density and highvelocity or high-viscosity flows, respectively. Joule heating enhances thermal energy generation and impacts heat transfer structures where thermal transportation is vital for protection, effectiveness, or physical performance. This effect is very important in mechanisms where overheating may result in device failure, inadequacy, or deprivation of materials. Joule heating is significant in industrial metallurgy and material processing, nuclear reactors, biomedical applications, conserving structures and thermal transport, and astrophysical space exploration. Viscous dissipation is more important as internal friction generates significant heat, especially in high-shear regions. Dissipation effects find applications in technology and engineering, for instance, aerospace systems, jet mechanical structures, space dynamics, car engines, etc. With such imperative significance, Swain et al. [8] explained the combined effects of energy dissipation and Ohmic on hydro-magnetic movement and past a continuous surface entrenched in a permeable membrane. Mishra and Kumar [9.10] analyzed the heat efficiency of reactive and dissipative magnetohydrodynamic (MHD) nanofluid transmit past a continuous sheet due to Joule heating. Tarakaramu et al. [11] inspected the effects of dissipative and Ohmic heating and on MHD nanofluid motion over a two-way extending sheet. Some additional related papers on energy dissipation and Joule heating are those of Wahid et al., Jayanthi and Niranjan, Rasool et al., Lund et al., and Ouyang et al. [12-16].

Radiative thermal propagation and heat generation/ absorption are crucial phenomena in fluid flow analysis, especially in high-temperature environments where they significantly impact heat transfer. These mechanisms are essential in various industrial applications, including power generation, aerospace engineering, automotive industry, electronics cooling, and chemical processing. Effective thermal management by controlling radiative heat transfer and absorption enhances system durability, energy efficiency, and operational reliability in these fields. Suresh Kumar et al. [17] performed an examination of a radiative MHD Casson nanofluid transport considering heat generation, the Hall effect, and activation energy via numerical solutions. The results of radiative mechanisms and higherorder reactive species on non-Darcy-assorted buoyancedriven MHD nanofluid transport with a variable heat source/sink were presented by Sarkar et al. [18]. Alharbi et al. [19] numerically scrutinized the effects of the radiative process on a bioconvective Maxwell-nanofluid transport in a widening sheet with thermal radiation considering exponential heat source/consumption. Explorations of Swain et al., Prakash et al., Khan et al., and Sekhar et al. [20-24]

provided a detailed inquiry on the radiative and heat-generating impact on hydro-magnetic nanofluid transport.

Chemical reaction effects on hydromagnetic nanofluid movement are of astonishing practical implication in engineering and technology fields. Plausible uses of this flow can come across in plentiful industrial procedures, for example, the power systems and chemical mechanisms. The study of reactive effects on MHD nanofluid flow via different shapes has been inspected using various arithmetical techniques. Sademaki et al. [25,26] included the effects of reactive species on hydromagnetic fluid transport and various physical flow parameters employing the finite difference method to find the solutions. Reddy et al. [27] discussed the effects of reactive species on radiative MHD Brinkman-type motion across a wavering permeable plate with a diffusion-thermo effect. Shamshuddin et al. [28] explored the outcomes of reactive species on radiative hydro-magnetic micropolar nanofluid transport incorporating activation energy and the Hall effect past an absorbent extending surface numerically. The studies of Shamshuddin et al., Patil et al., Hussain et al., and Khan et al. [29-32] are worth mentioning due to their inclusion of reactive processes in the MHD nanofluid transport regime with diverse stream geometries. The thermal and solutal flow study in Casson fluids has significant industrial applications. Shamshuddin et al. [33] studied Casson fluid's thermal and reactive properties at stagnation point movement past a radiative, reactive sheet. Similarly, Ibrahim et al. [34] discussed how species interactions and thermal sources affected the dissipative magnetized flow of Casson nanofluids over a nonlinear permeable surface. Brewster [35] deliberated thermal radiative characteristics, while Liao [36] scrutinized the "Homotopy Analysis Method" for solving nonlinear system of equations. Nadeem et al. [37] researched the MHD Casson nanofluid movement along convective circumstances.

"Response Surface Methodology (RSM)" is a statistical and arithmetical technique for modeling and analyzing models in which numerous variables influence the response of interest. It optimizes procedures by analyzing the correlations amid input variables and intended output, making it excellent for situations in which multiple factors influence the response. This methodology is very useful for determining optimal conditions and enhancing system performance, making it extensively relevant in engineering, manufacturing, and product design. Mishra et al. [38] presented the sensitivity of improved heat movement in Eyring Powell nanofluid transport, specifically across a convective radiating Riga plate with irregular heat sources and flux constraints. Similarly, Pattnaik et al. [39] used RSM to optimize the heat transfer rate in micro-structured fluid

flow via a permeable contracting surface, addressing free convection processes. Ontela et al. [40] expanded the research by exploring thermal flow optimization and sensitivity study in hybridized fluid movement across a radiative sheet, highlighting possible implications in solar-powered charging stations. Faroog et al. [41] and Waqas et al. [42] highlighted enhanced heat transfer capabilities of silver-based hybrid nanofluids in industrial and biomedical applications. Algawasmi et al. [43] and Mishra [44] investigated flow behavior under nonlinear heat sources and radiative influences, while Mishra et al. [45] employed neural networks to model heat transfer across various geometries. Mishra and Kumar [10] further analyzed MHD nanofluid flow incorporating slip conditions and Joule heating effects.

# 1.1 Research gap analysis

Based on the aforementioned literature assessment following key features that fill the gap of the existing research work:

- · Existing literature on Casson nanofluids has not focused on the joint impact of Ohmic heating and heat generation; therefore, the present study analyzes the aforementioned factors in the hydromagnetic transport of Casson nanofluids past a nonlinear oblique absorbent surface.
- · The impact of Ohmic heating on viscoplastic nanofluids, particularly in conjunction with MHD and heat transfer, has not been explored in the existing literature; therefore, the energy transfer efficiency in thermal systems enhances the incorporation of Ohmic heating.
- To address the gap in the analysis of Grashof number (Gr), Casson parameter ( $\alpha$ ), and Brownian motion parameter (Nb) and thermophoresis which are not discussed earlier, are presented in the flow phenomena for the enhanced flow properties.

# 1.2 Novelty

Few of the following aspects lead to the work's novelty:

- · It introduces the vast analysis of MHD Casson nanofluid flow over a permeable expanding surface, explored in prior viscoplastic nanofluid studies.
- The integration of Joule heating within the Casson-type non-Newtonian nanofluid that significantly impacts the thermal characteristics and the present model from the existing Newtonian or power-law nanofluid.

 The two-phase model equipped with both Nb and thermophoresis, which are essential for accurate modeling of nanoparticle dispersion in solar-based energy conversion.

# 2 Model description

This exploration extends electrically conducting viscousincompressible MHD 2D steady state Casson nanofluid assorted convective movement via an angle elevated nonlinear penetrable elongating sheet positioned at the x-axis. The velocity  $U_{\rm w}=px^{\frac{n-1}{2}}(p>0)$  of the surface deviates from the track of the x-axis and along the y-axis with the velocity of  $v = v_w$ . Moreover, the present transport regime is positive (y > 0). Additionally, this sheet is regularly executed with the equivalence  $B(x) = B_0 x^{\frac{n-1}{2}}$  by a magnetic strength, which is in the pathway of y-axis, as shown in Figure 1. The matching magnetic field persuades the electrically conducting fluid. It ought to be specified that the persuaded magnetic field approaches zero if the Reynolds number is enormously slight. To extend the wall so that the base remains fixed, whereas two undistinguishable and opposite forces are included along the x-axis path. In this,  $T_{\rm w}$  and  $C_{\rm w}$  are the measured temperature and concentration of nanoparticles, respectively, and as  $\to \infty$ , the temperature and nanoparticle volume fraction ambient values are  $T_{\infty}$  and  $C_{\infty}$ , respectively. Along with the impacts of heat generation and Joule heating, the analysis also takes dissipation and suction into account. Assuming the rheological equation of non-Newtonian Casson fluid as [33]

$$\tau = \tau_0 + \mu \alpha^*$$

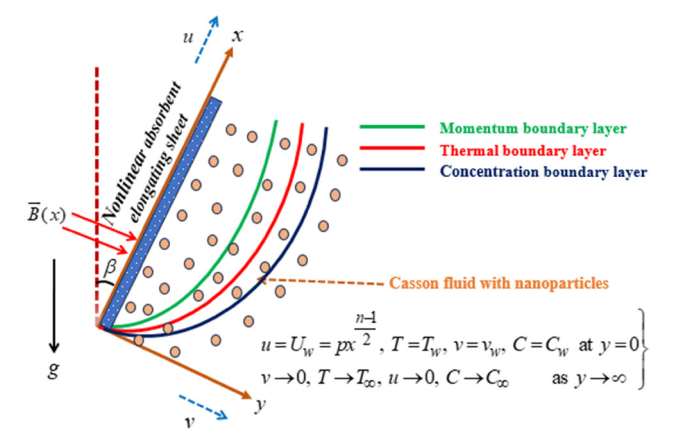


Figure 1: Geometrical model of the considered flow.

Λì

$$\tau_{ij} = \begin{cases} 2 \left[ \mu_{\rm B} + \frac{p_{\rm y}}{\sqrt{2\pi}} \right] e_{ij}, \, \pi > \pi_{\rm c} \\ 2 \left[ \mu_{\rm B} + \frac{p_{\rm y}}{\sqrt{2\pi_{\rm c}}} \right] e_{ij}, \, \pi < \pi_{\rm c} \end{cases}.$$

In the above equation,  $\mu_{\rm B}$  is the dynamic viscosity of the Casson fluid,  $p_{\rm y}$  is the fluid yield stress,  $\pi$  is the product of deformation rate components, expressed as  $\pi = e_{ij}e_{ij}$ , where  $e_{ij}$  is the (i,j)th components of the deformation rate, and  $\pi_{\rm c}$  is the critical value of  $\pi$ .

$$e_{ij} = \frac{1}{2} \left( \frac{\partial v_i}{\partial x_j} + \frac{\partial v_j}{\partial y_i} \right).$$

The equations that govern the previously indicated flow system near the oblique stretching surface are expressed as [34]:

$$\frac{\partial u}{\partial x} + \frac{\partial v}{\partial y} = 0, (1)$$

$$u\frac{\partial u}{\partial x} + v\frac{\partial u}{\partial y} = v\left(1 + \frac{1}{\alpha}\right)\frac{\partial^{2} u}{\partial y^{2}} - \frac{\sigma B^{2}(x)}{\rho_{f}}u$$

$$+ (g\beta^{T}(T - T_{\infty}) + g\beta^{C}(C - C_{\infty}))\cos\beta,$$
(2)

$$u\frac{\partial T}{\partial x} + v\frac{\partial T}{\partial y} = \gamma \frac{\partial^{2} T}{\partial y^{2}} + \frac{(\rho c)_{p}}{(\rho c)_{f}} \left[ \frac{D_{T}}{T_{\infty}} \left( \frac{\partial T}{\partial y} \right)^{2} + D_{B} \frac{\partial C}{\partial y} \frac{\partial T}{\partial y} \right] + \frac{\upsilon}{c_{p}} \left[ 1 + \frac{1}{a} \left( \frac{\partial u}{\partial y} \right)^{2} + \frac{\sigma B^{2}(x)}{(\rho c)_{f}} u^{2} \right] - \frac{1}{(\rho c)_{f}} \left( \frac{\partial q_{r}}{\partial y} \right) + \frac{1}{(\rho c)_{f}} \left[ Q_{s}(T - T_{\infty}) \right]$$
(3)

$$u\frac{\partial C}{\partial x} + v\frac{\partial C}{\partial y} = D_{\rm B} \left[ \frac{\partial^2 C}{\partial y^2} \right] + \frac{D_T}{T_{\infty}} \left[ \frac{\partial^2 T}{\partial y^2} \right] - k_{\rm r}(C - C_{\infty}). \quad (4)$$

They are connected to the following initial and boundary conditions:

$$u = U_{w} = px^{\frac{n-1}{2}}, T = T_{w}, v = v_{w}, \quad C = C_{w} \text{ at } y = 0 \\ v \to 0, \quad T \to T_{\infty}, \quad u \to 0, \quad C \to C_{\infty} \text{ as } y \to \infty$$
 (5)

where  $B(x) = B_0 x^{\frac{n-1}{2}}$  is an inconstant magnetic field.

The radiative thermal flux  $q_{\rm r}$  with the Rosseland approximation was deduced by Brewster [35], expressed as

$$q_{\rm r} = -\frac{4\sigma^{\rm s}}{3A_{\rm c}} \frac{\partial T^{\prime 4}}{\partial y^{\prime}},\tag{6}$$

where  $\sigma^s$  and  $A_c$  denote, respectively, the Stefan–Boltzmann constant and mean absorption coefficient. Letting a slight temperature change between the fluid temperature T and

free stream temperature  $T_{\infty}'$  is expanded as a linear function about a free transport temperature  $T_{\infty}$  after ignoring the second and higher-order terms in  $(T - T_{\infty})$  produces as a result of the form;

$$T^4 \cong 4T_{\infty}^3 T - 3T_{\infty}^4. \tag{7}$$

Using equations (6) and (7), equation (3) yields

$$u\frac{\partial T}{\partial x} + v\frac{\partial T}{\partial y} = y\frac{\partial^{2}T}{\partial y^{2}} + \frac{(\rho c)_{p}}{(\rho c)_{f}} \left[ \frac{D_{T}}{T_{\infty}} \left( \frac{\partial T}{\partial y} \right)^{2} + D_{B} \frac{\partial C}{\partial y} \frac{\partial T}{\partial y} \right] + \frac{\upsilon}{c_{p}} \left[ 1 + \frac{1}{\alpha} \left( \frac{\partial u}{\partial y} \right)^{2} + \frac{\sigma B^{2}(x)}{(\rho c)_{f}} u^{2} \right] + \frac{1}{(\rho c)_{f}} \left[ \frac{16\sigma^{s}}{3A_{c}} \frac{\partial}{\partial y} \left( T^{3} \frac{\partial T}{\partial y} \right) \right] + \frac{1}{(\rho c)_{f}} \left[ Q_{s}(T - T_{\infty}) \right]$$
(8)

To transmute the set of partial differential equations (PDEs) (equations (3)–(6)), we apply the following similarity parameters following Ibraham et al. [34]

$$\eta = y\sqrt{\frac{n+1}{2\nu}}x^{\left(\frac{n-1}{2}\right)}, \psi = \sqrt{\frac{2p\nu}{n+1}}x^{\left(\frac{n-1}{2}\right)}f(\eta),$$

$$\nu = -\sqrt{\frac{p\nu(n-1)}{2}}x^{\left(\frac{n-1}{2}\right)}\left[f(\eta) + \frac{n-1}{n+1}nf'(\eta)\right]$$

$$u = px^{\left(\frac{(n-1)}{2}\right)}f'(\eta), \phi(\eta) = \frac{C - C_{\infty}}{C_{w} - C_{\infty}}, \theta = \frac{T - T_{\infty}}{T_{w} - T_{\infty}}$$
(9)

where  $\psi, \eta, f(\eta), \theta(\eta)$ , and  $\phi(\eta)$  are the stream function, local similarity variable, non-dimensional stream function, non-dimensional temperature, and non-dimensional concentration, respectively, Standard equations of the stream function  $\psi$  are defined as  $u = \frac{\partial \psi}{\partial y}$  and  $v = -\frac{\partial \psi}{\partial x}$ 

By the use of equation (9), the PDEs are transformed into the following ordinary differential equations (ODEs):

$$\left(1 + \frac{1}{\alpha}\right) f''' + ff'' - \text{Ha}f' - \frac{2n}{n+1} f'^{2} - \frac{2}{n+1} (\text{Gm}\phi - \text{Gr}\theta) \cos\beta = 0,$$
(10)

$$\left(\frac{3+4\mathrm{Nr}}{3}\right)\theta'' + \mathrm{Pr}\left[f\theta' + \mathrm{Nt}\theta'^2 + \mathrm{Nb}\theta'\phi' + J_{\mathrm{H}}f'^2 + Q_0\theta + \left(1 + \frac{1}{\alpha}\right)\mathrm{Ec}f''^2\right] = 0,$$
(11)

$$\phi'' + \frac{Nt}{Nb}\theta'' + Le \Pr(f\phi' - Kc\phi) = 0.$$
 (12)

The transformed initial and borderline settings are given by

$$f(\eta) = S, \quad f'(\eta) = 1, \, \theta(\eta) = 1, \, \phi(\eta) = 1 \text{ at } \eta = 0$$

$$f'(\eta) = 0, \, \theta(\eta) = 0, \, \phi(\eta) = 0 \text{ as } \eta \to 0$$

$$, \quad (13)$$

where prime denotes  $\frac{d}{dn}$ 

$$Gr = \frac{g\beta^{T}(T_{W} - T_{\infty})}{p^{2}x^{(2n-1)}}, Gm = \frac{g\beta^{C}(C_{W} - C_{\infty})}{p^{2}x^{(2n-1)}},$$

$$Ha = \frac{2\sigma B_{0}^{2}}{p\rho_{f}(n+1)}, Nt = \frac{(\rho c)_{p}D_{T}(T_{W} - T_{\infty})}{v(\rho c)_{f}},$$

$$Pr = \frac{v}{v}, y = \frac{k}{(\rho c)_{f}}, Ec = \frac{U_{W}^{2}}{(T_{W} - T_{\infty})c_{p}},$$

$$Nb = \frac{(\rho c)_{p}D_{B}(C_{W} - C_{\infty})}{v(\rho c)_{f}}, J_{H} = Ec$$

$$Ha = \frac{2\sigma B_{0}^{2}U_{W}}{p\rho_{f}(T_{W} - T_{\infty})c_{p}(n+1)},$$

$$S = -\frac{v_{W}}{\sqrt{\frac{p(n+1)v}{2}}x^{\left(\frac{n-1}{2}\right)}}, Kc = \frac{2xk_{r}}{(n+1)U_{W}},$$

$$Q_{0} = \frac{2xQ_{S}}{(\rho c)_{f}(n+1)U_{W}}, Nr = \frac{4\sigma^{S}T_{\infty}^{3}}{A_{c}k}, Le = \frac{y}{D_{B}}.$$

The dimensional engineering curiosity connected to the problem is as follows:

Local wall friction coefficient  $S_f = \frac{\mu_B}{\rho U_w^2} \left[ 1 + \frac{1}{\alpha} \left\| \frac{\partial u}{\partial y} \right\|_{\infty} \right]$ 

Rate of heat transport  $NU_X = \frac{xq_w}{l_{t}(T-T)}$ 

Rate of mass transport  $Sh_X = \frac{xq_m}{D_R(C_w - C_m)^2}$ 

where  $q_{\rm w}$  is the heat flux given by  $q_{\rm w} = \left| -\left[k + \frac{16\sigma^{s}T_{\rm w}^{3}}{3A_{\rm c}}\right]\left(\frac{\partial T}{\partial y}\right]\right|$ 

and  $q_{\rm m}$  is the mass flux given by  $q_{\rm m} = -D_{\rm m} \left| \frac{\partial C}{\partial y} \right|_{y=0}$ 

Utilizing the similarity parameters in equation (9), the dimensionless engineering quantities can be reduced as:

$$Re_{x}^{\frac{1}{2}}Sf_{x} = \sqrt{\frac{2}{n+1}} \left( 1 + \frac{1}{\alpha} \right) f''(0),$$

$$Re_{x}^{-\frac{1}{2}}Nu_{x} = -\sqrt{\frac{2}{n+1}} \left( \frac{3+4Nr}{3} \right) \theta'(0),$$

$$Re_{x}^{-\frac{1}{2}}Sh_{x} = -\sqrt{\frac{2}{n+1}} \phi'(0)$$
(15)

where the local Reynolds number is expressed as  $Re_x = \frac{U_w x}{v}$ .

# 3 Numerical method of solution

Equations (10)-(13) used to simulate this inherently nonlinear Casson nano-fluid flow across a nonlinear inclined stretched sheet employing the boundary value problem. Normally, getting closed-form outcomes is rather 6 — MD. Shamshuddin et al. DE GRUYTER

challenging. To find the right consequences, a numerical procedure that applies the Runge–Kutta technique and the shooting approach is utilized. The Runge–Kutta technique is a well-known family of iterative methods for approximating ODE solutions. Now, the BVP is converted to IVP by converting into first-order ODEs, as described below, along with a flow chart procedure (Figure 2)

$$f = J_{1}, \quad f' = J_{2}, \quad f'' = J_{3}, \quad f''' = J'_{3},$$

$$\theta = J_{4}, \quad \theta' = J_{5}, \theta'' = J'_{5},$$

$$\phi = J_{6}, \phi' = J_{7}, \phi'' = J'_{7}$$
(16)

Incorporating equation (16) in equations (10)–(12) leads to first-order ODEs as follows:

$$J'_{3} = \frac{1}{\left(1 + \frac{1}{a}\right)} \left[ \text{Ha} J_{2} + \frac{2n}{(n+1)} J_{2}^{2} + \frac{2}{(n+1)} (\text{Gm} J_{6} - \text{Gr} J_{4}) \cos \beta - J_{1} J_{3} \right], \tag{17}$$

$$J_{5}' = -\frac{\Pr}{\left(\frac{3+4Nr}{3}\right)} \left[ J_{1}J_{5} + NtJ_{5}^{2} + NbJ_{5}J_{7} + J_{H}J_{2}^{2} + Q_{0}J_{4} + \left(1 + \frac{1}{\alpha}\right) EcJ_{3}^{2} \right],$$
(18)

$$J'_{7} = -\frac{Nt}{Nb} \left[ -\frac{Pr}{\left(\frac{3+4Nr}{3}\right)} \left[ J_{1}J_{5} + NtJ_{5}^{2} + NbJ_{5}J_{7} + J_{H}J_{2}^{2} \right] + Q_{0}J_{4} + \left[ 1 + \frac{1}{\alpha} \right] EcJ_{3}^{2} \right] - Le Pr(J_{1}J_{7} - KcJ_{6})$$
(19)

Leading boundary conditions

$$J_{1}(\eta) = S, \quad J_{2}(\eta) = 1, \quad J_{4}(\eta) = 1,$$

$$J_{6}(\eta) = 1, \text{ at } \eta = 0,$$

$$J_{2}(\eta) \to 0, \quad J_{4}(\eta) \to 0, \quad J_{6}(\eta) \to 0, \text{ as } \eta \to 0.$$
(20)

The appropriate guesstimate values are selected, and integration is then carried out. Thus, the appropriate step size  $\Delta \eta = 0.001$  is selected.

### 3.1 Method validation

A comparison of the studied outcomes with previously published work is provided in Table 1. This resemblance indicates that the current results align very well with the investigations of Liao [36] and Nadeem *et al.* [37] for  $-\theta'(0)$ 

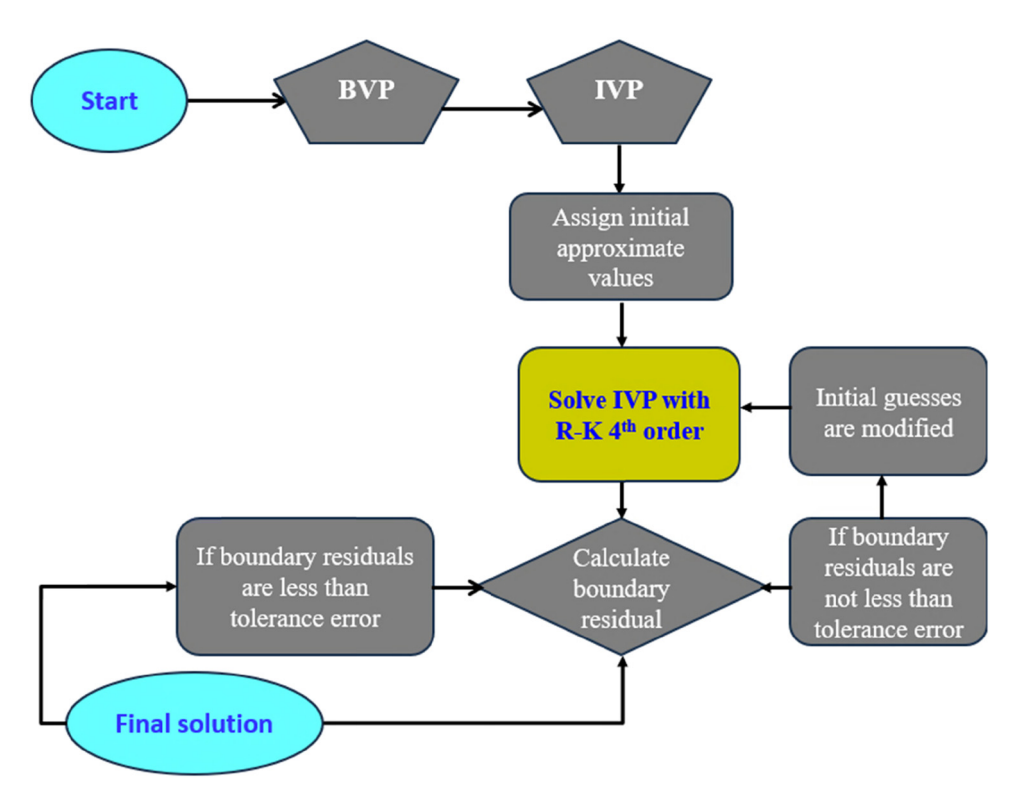


Figure 2: Numerical methodology flow chart.

0.72487

0.7248

n	Nt	Nt	Liao	[36]	Nadeer	n <i>et al.</i> [37]	Pro	esent
		$-\theta'(0)$	$-\phi'(0)$	$-\theta'(0)$	-φ'(0)	− <i>θ</i> ′(0)	$-\phi'(0)$	
0.2	0.3	0.4533	0.8395	0.452	0.8402	0.45235	0.84025	
	0.5	0.3999	0.8048	0.3987	0.8059	0.39874	0.80535	
0.3	0.3	0.4282	0.7785	0.4271	0.7791	0.42711	0.77913	
	0.5	0.3786	0.8323	0.3775	0.739	0.3776	0.73987	
10	0.3	0.4277	0.7654	0.4216	0.766	0.42164	0.76615	

0.3728

**Table 1:** Comparison of  $-\theta'(0)$  and  $-\phi'(0)$  for different values of n and Nt

and  $-\phi'(0)$ , demonstrating the exactness and consistency of the considered computational technique to solve governing equations. The slight deviations observed are attributed to differences in numerical methods.

0.3739

0.7238

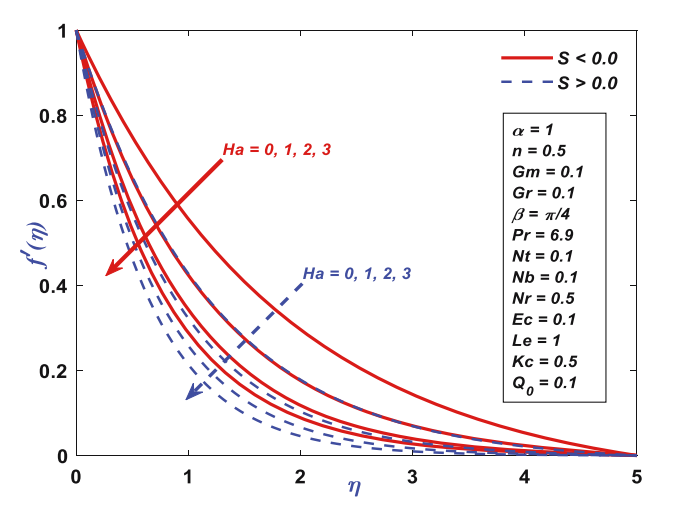
# 4 Discussion and outcomes

0.5

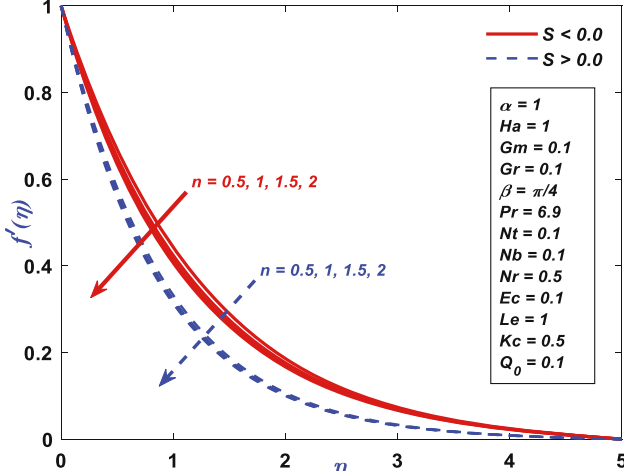
To comprehend the physical insight of the modeled problem, the effects of various pertinent parameters fused in the problem on the nanofluid momentum, temperature, and concentration are delineated graphically. Shear stress, Nusselt number, and Sherwood number are computationally solved and exhibited in tabular format. The arithmetical computations have been done by considering the constant values of various incorporated parameters in the flow structure that are well displayed in the graphs.

Figure 3 exhibits the effects of Hartmann number Ha on the fluid velocity. The variation of the factor Ha within the flow domain is presented for the consideration of the standard range described as  $0 \le \text{Ha} \le 3$ . In general, the numerically assigned value of Ha, Ha = 0, depicts the non-occurrence of the magnetization on the flow profile, while the nonzero variation portrays the characteristic of the magnetization on the fluid velocity. It is stated that enhancing Ha diminishes fluid velocity. The reason behind this circumstance is the Ha lessens the fluid velocity by strengthening the magnetic damping properties (Lorentz force), which work as an added drag on the fluid regime. The occurrence of the resistivity generated from the Lorentz force is due to the inclusion of applied magnetization in the momentum distribution. This results in lower velocities near the walls presenting a thinner bounding surface thickness leading to shrink nanofluid velocity. This behavior is exhibited in two distinct folds, such as S > 0 leading the case of suction and S < 0 showing the behavior of injection. The comparative analysis displays that suction is more pronounced to attenuate the fluid velocity. Figure 4 displays the influence of a non-linear stretching parameter n on fluid velocity where the behavior is depicted for the particular range of *n* as  $0.5 \le n \le 2$ . It is detected that

0.37286



**Figure 3:** Velocity profile performance toward the magnetic field (M).



**Figure 4:** Velocity profile performance toward n.

MD. Shamshuddin et al.

DE GRUYTER

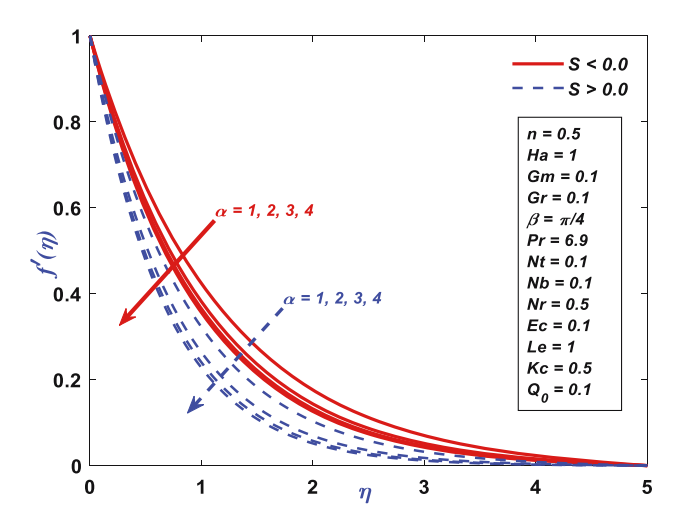


**Figure 5:** Velocity profile performance toward  $\alpha$ .

improving n decelerates the fluid pace. Physically, the nonlinear stretching parameter drops the fluid velocity by snowballing the viscid drag and deepening the boundary stratum, which mutually produce superior opposition to fluid movement near the elongating surface. The outcome inclusively lessens the fluid velocity in the borderline layer domain. Figure 5 showcases the distinction of the Casson parameter  $\alpha$  on fluid velocity and to show the characteristic, the numerical variation of the factor is presented as  $1 \le \alpha \le 4$ . It noticed that mounting  $\alpha$  depresses the fluid velocity. This is because  $\alpha$  rises the fluid's yield stress, which brings resistance toward the flow regime. As  $\alpha$ upsurges, the fluid needs a strong force to begin moving, inspissation of the boundary layer, and dipping of the shear rate, hence the velocity drop occurs. The influence of thermal Grashof number (Gr) on fluid velocity is

showcased in Figure 6, in which the variation of Gr is reported within the standard range of  $0 \le Gr \le 3$ . The assignment Gr = 0 clarifies the absence of buoyancy, whereas the effect of buoyancy is deployed for its nonzero variation. Physically, the buoyancy occurs for the density variation between the layers of the fluid, which leads to pressure variation. The observation reveals that the pressure at the bottom layer is dominated by the pressure at the top which shows buoyancy. Here, the positive variation of Gr indicates the cooling of the surface since the temperature transfers from the surface toward the ambient state of low temperature region. It is seen that mounting Gr escalates the fluid momentum. The cause behind this is Gr enumerates the supremacy of buoyancy forces over viscidness in free convective motions. As the Gr upsurges, the buoyancy forces become tougher, generating more dynamic convective currents, hence improving the fluid pace. Figure 7 illustrates the impact of Gm on fluid velocity with a significant variation of the factor as  $0.5 \le Gm \le 2$ . In this case, the variation is presented due to the concentration difference, and the positive variation of the factor shows the concentration at the surface is higher than that of the ambient state. It is noted that the fluid speed decreases when Gm is elevated. This is because Gm shrinks the fluid speed when the mass buoyancy forces engendered by concentration gradients resist the heat buoyancy forces, forming an opposition to the fluid stream. In this situation, the interface amid solutal and heat buoyancy effects can diminish the complete generative force for fluid transport, causing high fluid pace. Figure 8 displays the variation of fluid velocity when adjusting the inclination angle  $\beta$ , which is reported as  $\pi/6 \le \beta \le \pi$ . Mathematically, the cosine value retards with the increase in the inclined angle, and it is observed that increasing  $\beta$  values reduce

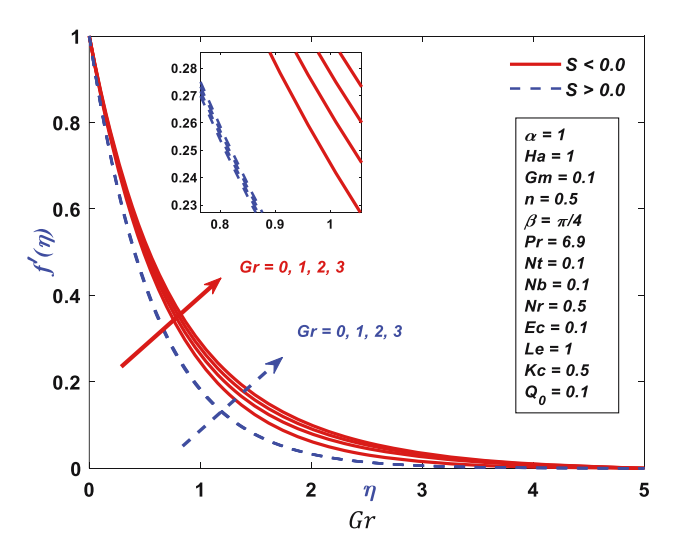


Figure 6: Velocity profile performance toward Gr.

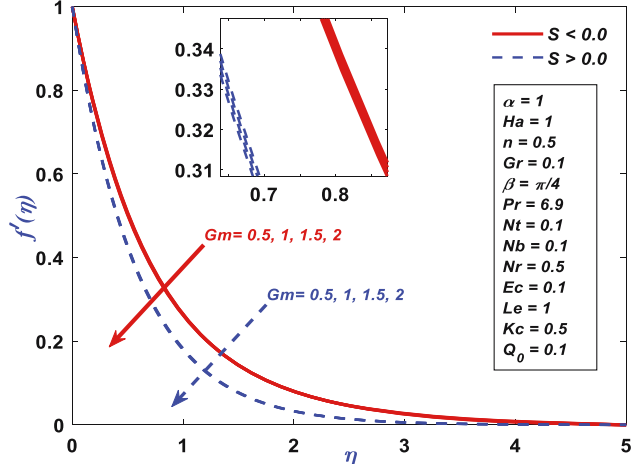
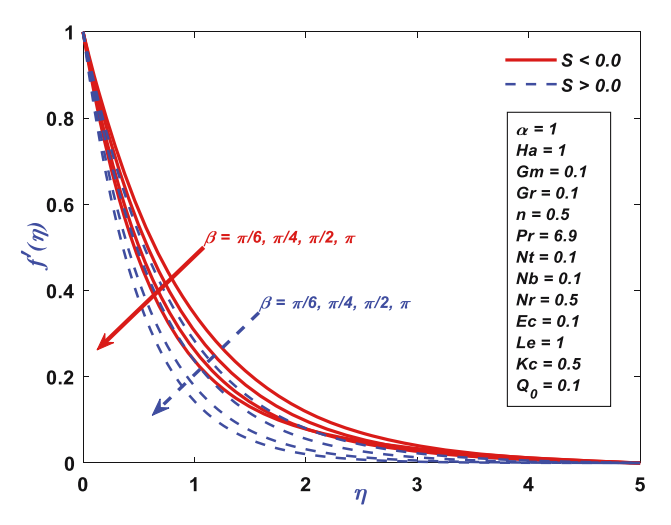
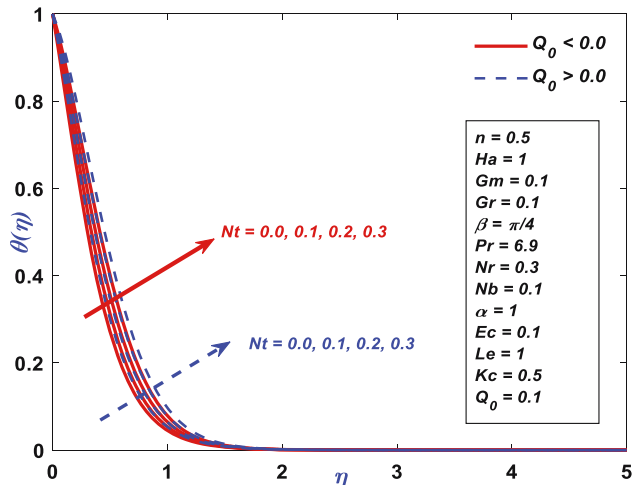


Figure 7: Velocity profile performance toward Gm.



**Figure 8:** Velocity profile performance toward  $\beta$ .



**Figure 10:** Temperature profile performance toward Nt.

the fluid momentum. The physics behind is the fact that the inclined angle of a surface disturbs the fluid velocity by fluctuating the gravitational forces, escalating the frictional resistance, and plummeting the buoyancy-driven convection, hence it tends to reduce the fluid pace.

Figure 9 presents the effect of radiation Nr on the fluid temperature, where the behavior is projected within the range of  $0 \le Nr \le 3$ . Particularly, Nr = 0 signifies the behavior of fluid temperature without the occurrence of radiative heat and the nonzero variation portrays the characteristic of thermal radiation. It realized those mounting values of Nr progresses the magnitude of thermal boundary layers by adding radiant energy to the fluid, which gives a snowballing effect on the fluid temperature. Figures 10 and 11 depict the influence of thermophoresis Nt and Nr0 Brownian motion parameter Nr1 on the fluid

temperature, respectively. The factor Nt is distributed within the certain range of  $0 \le Nt \le 3$ , and Nb is presented as  $0.1 \le Nb \le 0.4$ . It is noticed that in both cases the temperature of the fluid increased. This is because both Nt and Nb increase the fluid temperature by enabling the re-dispersion of heat via thermophoresis and augmenting heat transport via Brownian movement. The collective outcomes yield more effective energy distribution, hence improving the fluid temperature. The random motion of the Brownian motion and the thermal gradient impact enhance the heat transport properties which encourage the thermal properties. Figure 12 illustrates the temperature demeanor for the response of Ec, where the factor is reported as  $0 \le Ec \le 0.3$ . In general, the numerical consideration of Ec = 0 shows the absence of dissipative heat on

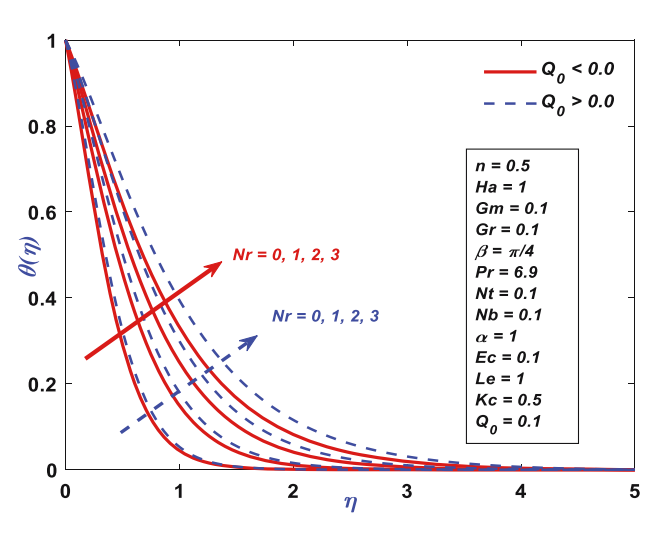
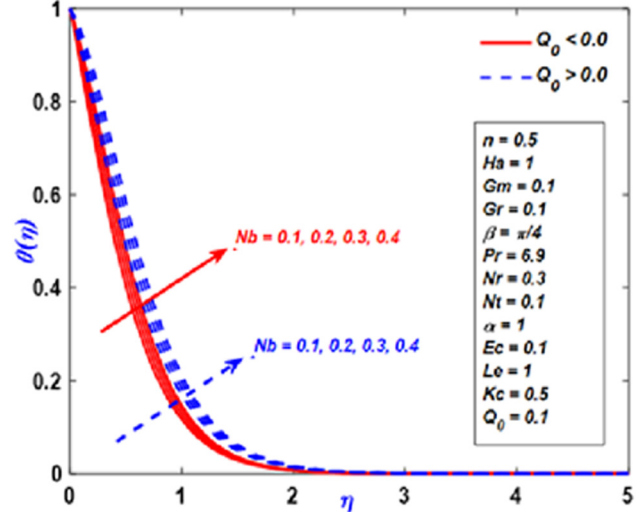


Figure 9: Temperature profile performance toward Nr.



**Figure 11:** Temperature profile performance toward Nb.

10 — MD. Shamshuddin et al. DE GRUYTER

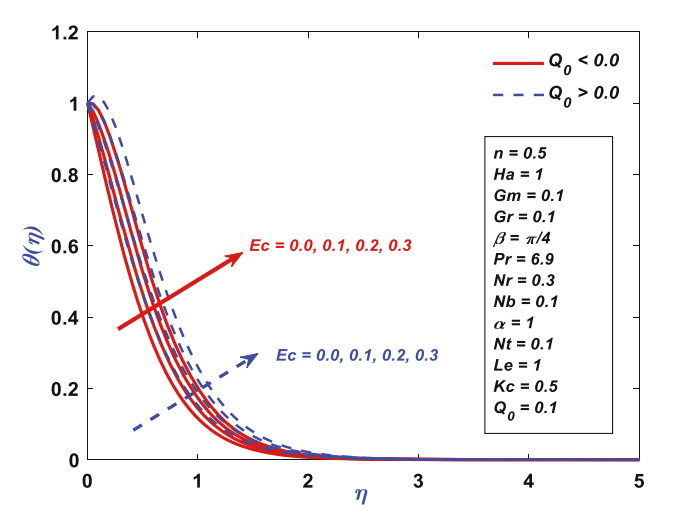


Figure 12: Temperature profile performance toward Ec.

the energy transport phenomena, and the nonzero variation indicates the role of dissipative heat affecting the fluid temperature. An increasing Ec boosts the energy of material particles due to high energy input stowed in the boundary stratum as an outcome enhances the temperature of the fluid.

Figure 13 demonstrates the influence of Schmidt number Le on the concentration profile, and the factor Le is projected within the standard range of  $1 \le Le \le 1.3$ . Physically, the factor Le described as the relationship between the thermal diffusivity and the Brownian diffusivity and the increasing order of Le shows a significant retardation in the Brownian diffusion. It is spotted that fluid concentration decreases as Le increases. Physically, the expansion of Le conveys higher thermal conductivity compared to mass diffusivity. In this case, the solutes in the

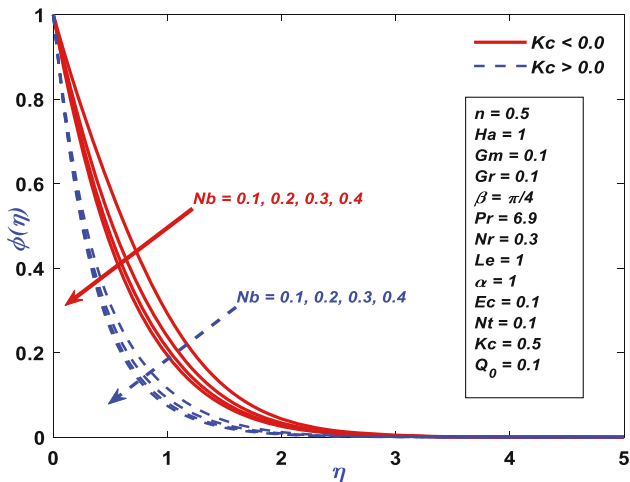


Figure 14: Concentration profile performance toward Nb.

fluid diffuse at a very low pace, leading to minimal effectiveness in solute transmission, sharper concentration gradients, and ultimately declining the fluid concentration. Figure 14 shows the variation of Brownian motion parameter Nb in fluid concentration. It is perceived that enhancing the Nb diminishes the fluid concentration. This is because boosting the Nb drops the fluid concentration as it augments the random motion of particles, resulting in superior dispersion and distribution all around the fluid. This condenses the gathering of particles and compresses concentration gradients, subsequently reducing the fluid concentration. Figure 15 displays the variation of thermophoresis on fluid concentration. It is perceived that enhancing the Nt improves the fluid concentration. The physics behind this is, higher Nt heightens the fluid concentration by triggering elements to move from warmer to cooler

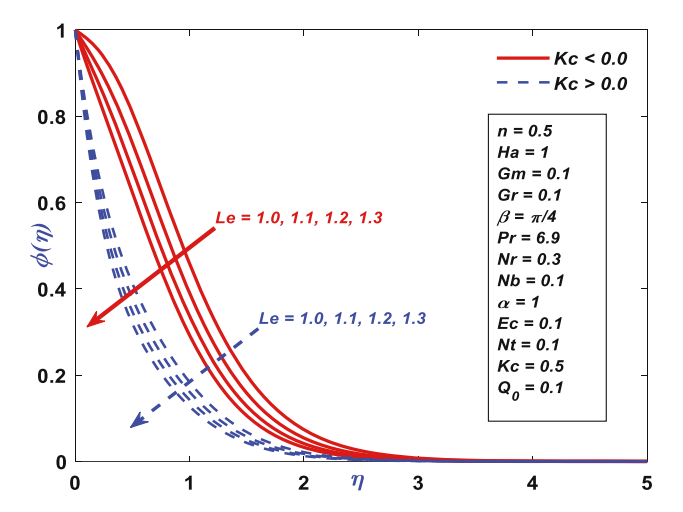


Figure 13: Concentration profile performance toward Le.

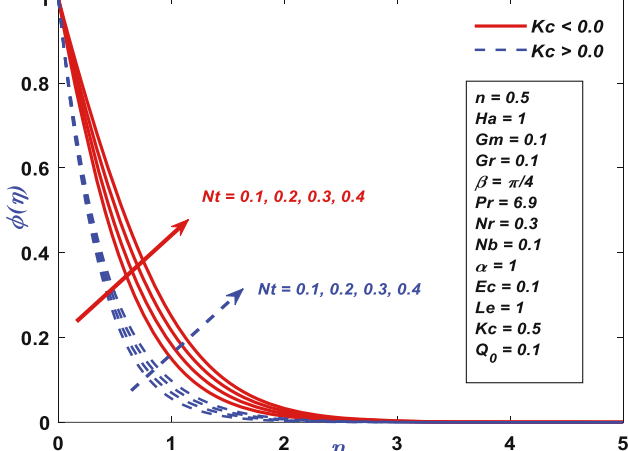


Figure 15: Concentration profile performance toward Nt.

points, resulting in accretion in cooler points. This effect leads to a deepening boundary stratum and high varying particle dispersion within the fluid, hence increasing the fluid concentration.

# 4.1 Drag friction coefficient, thermal flow rate, and solutal flow rate

The variation of the drag friction coefficient of Casson nanofluid with various parameters is exhibited in Table 2. It is professed from this table that the wall friction rises with the intensification in Gr and  $\alpha$ , but it lessens with Ha,  $\beta$ , S, Gm, and  $\varphi$ . The rate of thermal transport rate variation with different parameters is shown in Table 3. It is acknowledged from this table that the Nusselt number upsurges with an increase in Nr, but a contrary trend is perceived with an escalation of Ec, Nb, Nt, and Q. The deviation of the Sherwood number is accessible in Table 4 for a diversity of parameters. The Sherwood number grows by expanding Le, Nb, Nt, and Kc.

#### 4.2 RSM

An enhanced and effective design is proposed for analyzing the thermal transport rate, a sophisticated statistical technique, which is presented in this section. To prepare

**Table 2:** Numerical values for drag friction coefficient with various parameter values

На	S	Gm	Gr	α	β	$Sf_{X}$
1						-2.0914
2						-2.4984
3						-2.8423
1	0.1					-2.6248
	0.2					-2.6781
	0.3					-2.7322
	0.1	0.1				-2.8423
		0.2				-2.8642
		0.3				-2.8861
		0.1	0.1			-2.8423
			0.2			-2.8187
			0.3			-2.7952
			0.1	1		-3.0874
				2		-2.7106
				3		-2.5714
				1	$\pi/4$	-2.8423
					$\pi/2$	-2.8441
					$\pi$	-2.8465

**Table 3:** Numerical values for heat transfer rate with various parameter values

Nr	Q	Nb	Nt	Ec	Nu <sub>x</sub>
1					1.3162
2					1.4641
3					1.5849
1	0.1				1.201
	0.2				1.0758
	0.3				0.9392
	0.1	0.1			1.0758
		0.2			0.8521
		0.3			0.6593
		0.1	0.1		1.0758
			0.2		0.9353
			0.3		0.8083
			0.1	0.1	1.6426
				0.2	1.0758
				0.3	0.5055

**Table 4:** Numerical values for mass transfer rate with various parameter values

Le	Nb	Nt	Kc	$Sh_X$
1				2.1991
1.1				2.4114
1.2				2.6186
1	0.1			2.1991
	0.2			2.5176
	0.3			2.6146
	0.1	0.1		2.1991
		0.2		1.9614
		0.3		1.9039
		0.1	0.1	1.6543
			0.2	1.8074
			0.3	1.9479

a predictive model, RSM is utilized for the response employing several characterizing factors. In particular, RSM is the assortment of both the arithmetical and statistical methods. Moreover, the major goal of the proposed discussion is to optimize the response which is characterized by several factors considered within their proper

Table 5: Range and their levels of factors for Nusselt number

Parameters		Level	
	Low (-1)	Medium (0)	High (1)
Nb	0.1	0.2	0.3
Nt	0.1	0.2	0.3
Nr	0.1	0.3	0.5

Table 6: Experimental design for heat transfer rate

Runs	tuns Real values		Response	Predicted fits	Predicted standard error fits	Percentile error	
	Nb	Nt	Nr	Nusselt number			
1	0.1	0.1	0.1	1.0758	1.07274	0.0020217	0.284038
2	0.3	0.1	0.1	0.6593	0.66087	0.0020217	-0.238786
3	0.1	0.3	0.1	0.8083	0.81002	0.0020217	-0.213327
4	0.3	0.3	0.1	0.4654	0.46300	0.0020217	0.514758
5	0.1	0.1	0.5	1.2041	1.20646	0.0020217	-0.196356
6	0.3	0.1	0.5	0.8266	0.82484	0.0020217	0.212398
7	0.1	0.3	0.5	0.9609	0.95929	0.0020217	0.167102
8	0.3	0.3	0.5	0.6395	0.64252	0.0020217	-0.472919
9	0.1	0.2	0.3	1.0123	1.01287	0.0015905	-0.056577
10	0.3	0.2	0.3	0.6490	0.64855	0.0015905	0.068917
11	0.2	0.1	0.3	0.9341	0.93497	0.0015905	-0.093430
12	0.2	0.3	0.3	0.7132	0.71245	0.0015905	0.104777
13	0.2	0.2	0.1	0.7320	0.73415	0.0015905	-0.294088
14	0.2	0.2	0.5	0.8928	0.89077	0.0015905	0.227069
15	0.2	0.2	0.3	0.8185	0.81846	0.0007804	0.005109
16	0.2	0.2	0.3	0.8185	0.81846	0.0007804	0.005109
17	0.2	0.2	0.3	0.8185	0.81846	0.0007804	0.005109
18	0.2	0.2	0.3	0.8185	0.81846	0.0007804	0.005109
19	0.2	0.2	0.3	0.8185	0.81846	0.0007804	0.005109
20	0.2	0.2	0.3	0.8185	0.81846	0.0007804	0.005109

range. The proposed technique is employed in describing the role of three distinct factors such as Nb, Nt, and Nr for the response of thermal flow rate, *i.e.* Nusselt number. The machine simulation process is supported for the ranges of these factors as Nb  $\in$  [0.1, 0.3], Nt  $\in$  [0.1, 0.3], and Nr  $\in$  [01, 0.5], respectively. The main goal of this technique is to find the effective role of the considered

three factors that maximize or minimize Nu. Particularly, machine design is developed by utilizing "Central Composite Design" (CCD) and BoxBehnken Design (BBD) in RSM, but for the proposed problem CCD is adopted for the robustness and efficiency. As per the design of the model, three different levels for each of the factors are considered, and these are generally low, medium, and

Table 7: ANOVA for heat transfer rate

Source	Degree of freedom	Adjusted sum of square	Adjusted mean of square	<i>F</i> -value	<i>P</i> -value	Coefficients
Model	9	0.520441	0.057827	11222.39	0.000	0.818458
Linear	3	0.516935	0.172312	33440.36	0.000	
Nb	1	0.331823	0.331823	64396.49	0.000	-0.182160
Nt	1	0.123788	0.123788	24023.39	0.000	-0.111260
Nr	1	0.061325	0.061325	11901.20	0.000	0.078310
Square	3	0.000825	0.000275	53.38	0.000	
Nb*Nb	1	0.000413	0.000413	80.15	0.000	0.01225
Nt*Nt	1	0.000076	0.000076	14.74	0.003	0.00525
Nr*Nr	1	0.000099	0.000099	19.18	0.001	-0.00600
Two-way interaction	3	0.002681	0.000894	173.45	0.000	
Nb*Nt	1	0.002103	0.002103	408.08	0.000	0.016212
Nb*Nr	1	0.000458	0.000458	88.79	0.000	0.007563
Nt*Nr	1	0.000121	0.000121	23.46	0.001	0.003888
Error	10	0.000052	0.000005			
Lack-of-fit	5	0.000052	0.000010			
Pure error	5	0.000000	0.000000			
Total	19	0.520493				

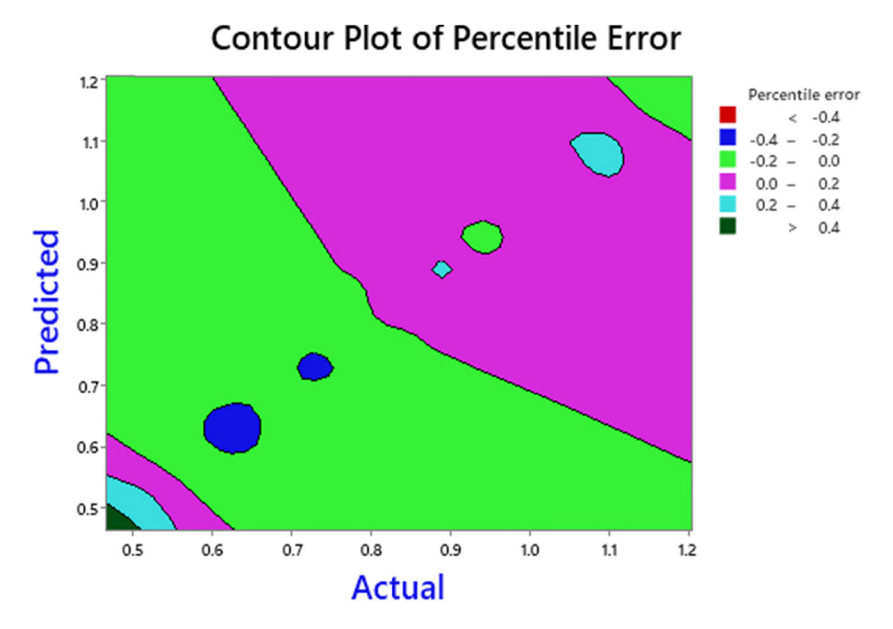


Figure 16: Contour profile for percentile error.

high, where each are coded as -1, 0, and 1, respectively. The range of each of the factor and their levels are presented in Table 5.

Table 6 based on the experimental set up for the methodology and then CCD is used to predict a design which contains a total of 20 experimental runts such as factorial, axial, and central points. For each combination of factors presented in Table 6, the

response of Nusselt number is recorded. The variation of the parametric values is presented based upon these 20 runs for which the calculation of the Nusselt number is obtained, which is called the observed values of the Nusselt number.

A statistical methodology, in particular analysis of variance (ANOVA) is used to determine the significance of factors involved in RSM. The procedure is conducted for the

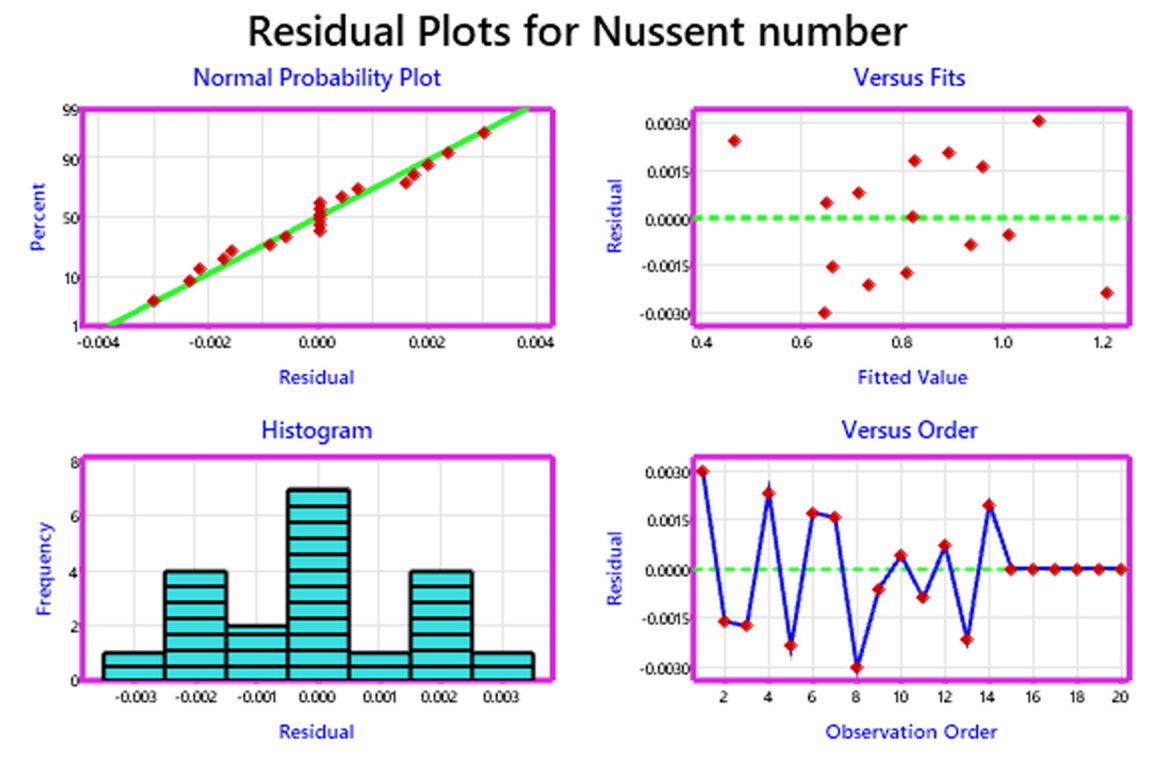


Figure 17: Residual profiles for Nusselt number.

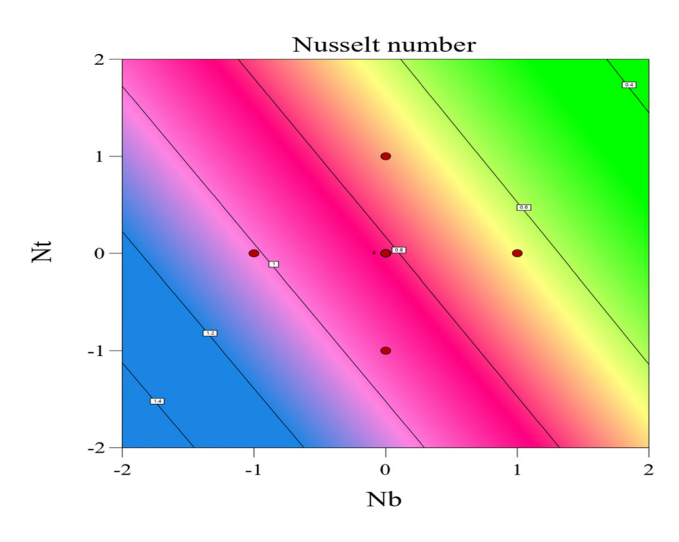


Figure 18: Contour plot of Nusselt number for Nb and Nt.

suitability of the machine criteria of a suitable choice of confidence interval of 95% or the significant level of 5%. For the proposed factors, the quadratic response surface model fit to the data collected from the experiment is expressed as

Nusselt number

 $= \begin{cases} 0.818458 - 0.182160Nb - 0.111260Nt + 0.078310Nr \\ + 0.01225Nb*Nb + 0.00525Nt*Nt - 0.00600Nr*Nr \\ + 0.016212Nb*Nt + 0.007563Nb*Nr + 0.003888Nt*Nr. \end{cases}$ 

The simulated F-values,  $F = MS_{Regression}/MS_{Residual}$ , were obtained and compared with the critical F-value at a significant level of 0.05 (Table 7). Here, the low p-values (p < 0.05) recommend that the model is significant. It reveals that the design of Nusselt number is dependent upon all the factors involved in it.

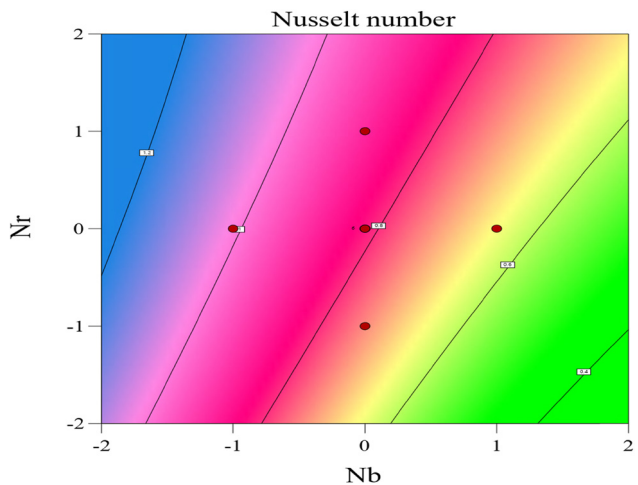


Figure 20: Contour plot of Nusselt number for Nb and Nr.

The adjusted  $R^2$  values in Table 7 indicate a well-fitted model to the data for which the quadratic model is suggested.

Figure 16 shows a contour profile representing the percentile error between the actual versus predicted values. The plot analyses the difference between the actual and predicted values considered in various ranges, using level curves to display the relationship between them. Percentile error quantifies the deviation within the actual and predicted values at particular levels. In the figure, the darker regions indicate higher errors, while lighter regions represent lower errors. The diagonal line signifies perfect predictions. Deviations from this diagonal are referred to as bias, the spread of points around it represents variance, and points far from the diagonal are considered outliers.

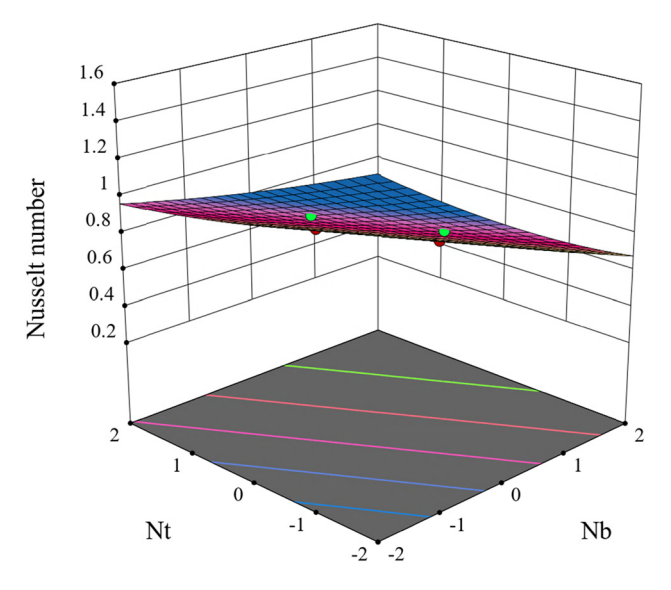


Figure 19: Surface plot of Nusselt number for Nb and Nt.

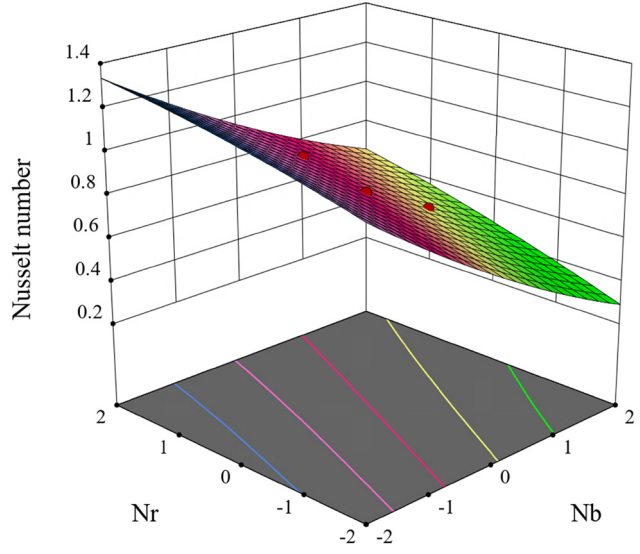


Figure 21: Surface plot of Nusselt number for Nb and Nr.

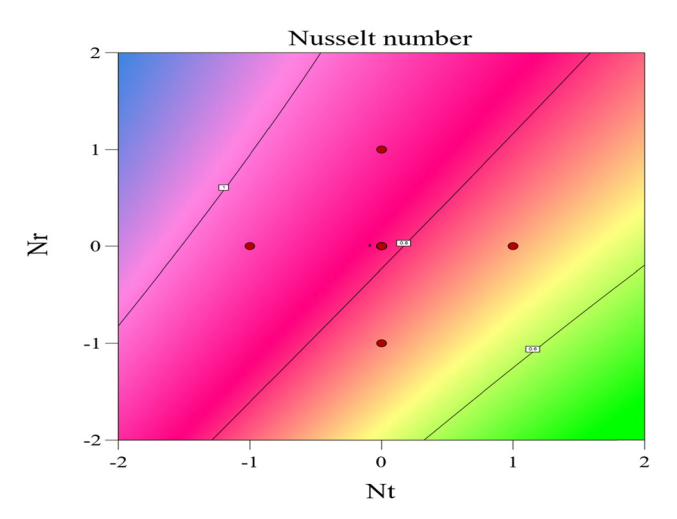


Figure 22: Contour plot of Nusselt number for Nr and Nt.

In general, residual plots are valuable tools for assessing the goodness of fit in a regression model. It represents the differences between predicted and actual values, and these variations are analyzed through residual plots. Figure 17 shows residual plots in four different levels. The normal probability plot is presented to evaluate whether the residuals follow a normal distribution for the fitted data. Since the residuals are approximately normally distributed, most data points lie close to a straight line, indicating the model's validity. The residual versus fitted value plot is employed to detect potential issues such as nonlinearity or unequal error variances. The histogram of residuals illustrates their distribution and checks for normality, showing a bell-shaped curve, which further confirms that the residuals against the

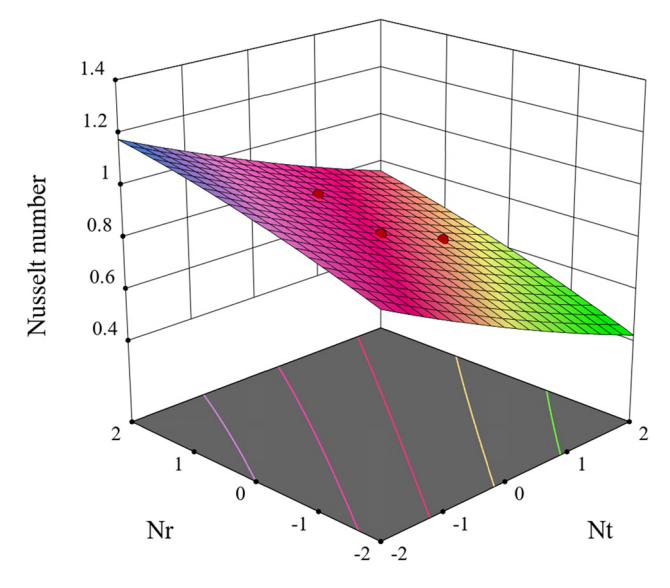


Figure 23: Surface plot of Nusselt number for Nr and Nt.

observation order is used to check for any patterns, ensuring the independence of observations.

Figures 18-23 show the graphical illustration for the Nusselt number utilizing the factors considering the values of these parameters. For each of the factors, the behavior of Nusselt number is depicted through contour and surface maps. These illustrate the Nusselt number and their prediction. In Figures 18 and 19, the effects of the factors Nt and Nt on the heat transfer rate considering the factor Rd at a central level are shown. It is shown that the response of Nusselt number retards the variations of both Nb and Nt. The factor in Figures 20 and 21 shows the role of Nb and Nr in the contour as well as surface plots for the Nusselt number, keeping Nt constant at a central value. There is a significant hike in the heat transfer rate, as depicted with increasing values of thermal radiation, but the Nb retards. In Figures 22 and 23, the contour vis-à-vis surface plots for the heat transfer rate are deployed, considering the variation of Nt and Nr. The factor Nt favors in decelerating the profile, whereas the reverse impact is rendered for the variation of Nr.

# 5 Conclusion

The current study intended to examine the Joule heating effects on steady reactive and dissipative MHD Casson nanofluid transport past a nonlinear inclined elongating absorbent sheet with heat generation. The model's leading highly coupled non-linear PDEs have been converted into ODEs using apposite similarity variables and then cracked numerically by the RungeKutta shooting technique. The results are abridged as follows:

- The velocity profile is escalated with expansion of Gr, while a converse trend is detected in enhancing Ha, n, Gm,  $\alpha$ , and  $\beta$ .
- The fluid temperature exhibited an upsurge with growing values of Nr, Nt, Ec, and Nb.
- The concentration trend of nanofluid upsurged with an increment in Nt, while Le and Nb exhibited the opposite outcome.
- The wall friction mounts with the growth in Grand $\alpha$ , but it lessens with Ha,  $\beta$ , S, Gm, and  $\varphi$ .
- The Nusselt number expands with an augmentation in Nr but a converse tendency is detected with an escalation of Ec, Nb, Nt, and O.
- The Sherwood number escalates on expanding Le, Nb, Nt, and Kc.

The flow model that we have examined is a simple case of geometry. Therefore, it would be interesting to perform in a 3D modeling of the problem, where the assumptions of parabolic shapes are not applicable. However, since this involves a simultaneous solution of a nonlinear system consisting of several PDEs, it requires a large and expensive computation time. Thus, it would be advantageous to develop computer programs based on COMSOL, as they provide fast and reliable solving approaches for such complex configurations.

**Funding information:** The authors state no funding involved.

**Author contributions:** All authors have accepted responsibility for the entire content of this manuscript and approved its submission.

**Conflict of interest:** The authors state no conflict of interest.

**Data availability statement:** The datasets generated and/ or analyzed during the current study are available from the corresponding author on reasonable request.

# References

- [1] Sakiadis BC. Boundary-layer behavior on continuous solid surfaces: I. Boundary-layer equations for two-dimensional and axisymmetric flow. AIChE J. 1961;7(1):26–8.
- [2] Crane LJ. Flow past a stretching plate. Z f
  ür Angew Math Phys (ZAMP). 1970;21:645–7.
- [3] Rama Devi SVV, Reddy MG. Parametric analysis of MHD flow of nanofluid in stretching sheet under chemical sensitivity and thermal radiation. Heat Transf. 2022;51(1):948–75. doi: 10.1002/htj. 22337.
- [4] Mabood F, Khan WA, Ismail AIM. MHD boundary layer flow and heat transfer of nanofluids over a nonlinear stretching sheet: A numerical study. J Magn Magn Mat. 2015;374:569–76.
- [5] Khan KA, Javed MF, Ullah MA, Riaz MB. Heat and Mass transport analysis for Williamson MHD nanofluid flow over a stretched sheet. Res Phys. 2023;53:106873. doi: 10.1016/j.rinp.2023.106873.
- [6] Sadighi S, Afshar H, Jabbari M, Ashtiani HAD. Heat and mass transfer for MHD nanofluid flow on a porous stretching sheet with prescribed boundary conditions. Case Stud Therm Eng. 2023;49:103345. doi: 10.1016/j.csite.2023.103345.
- [7] Adel M, Khader MM, Ahmad H. MHD nanofluid flow and heat transfer caused by a stretching sheet that is heated convectively: An approximate solution using ADM. Case Stud Therm Eng. 2024;60:104683. doi: 10.1016/j.csite.2024.104683.
- [8] Swain BK, Parida BC, Kar S, Senapati N. Viscous dissipation and Joule heating effect on MHD flow and heat transfer past a stretching sheet embedded in a porous medium. Heliyon. 2020;6(10):e05338. doi: 10.1016/j.heliyon.2020.e05338.
- [9] Mishra A, Kumar M. Thermal performance of MHD nanofluid flow over a stretching sheet due to viscous dissipation, Joule heating

- and thermal radiation. Int J Appl Comput Math. 2020;6(4):123. doi: 10.1007/s40819-020-00869-4.
- [10] Mishra A, Kumar M. Velocity and thermal slip effects on MHD nanofluid flow past a stretching cylinder with viscous dissipation and Joule heating. SN Appl Sci. 2020;2(8):1350. doi: 10.1007/s42452-020-3156-7.
- [11] Tarakaramu N, Satya Narayana PV, Babu DH, Sarojamma G, Makinde OD. Joule heating and dissipation effects on magnetohydrodynamic couple stress nanofluid flow over a bidirectional stretching surface. Int J Heat Technol. 2021;39(1):205–12.
- [12] Wahid NS, Arifin NM, Pop I, Bachok N, Hafidzuddin MEH. MHD stagnation-point flow of nanofluid due to a shrinking sheet with melting, viscous dissipation and Joule heating effects. Alex Eng J. 2022;61(12):12661–72.
- [13] Jayanthi S, Niranjan H. Effects of Joule heating, viscous dissipation, and activation energy on nanofluid flow induced by MHD on a vertical surface. Symmetry. 2023;15(2):314. doi: 10.3390/ sym15020314.
- [14] Rasool G, Wang X, Yashkun U, Lund LA, Shahzad H. Numerical treatment of hybrid water based nanofluid flow with effect of dissipation and Joule heating over a shrinking surface: Stability analysis. J Magn Magn Mat. 2023;571:170587. doi: 10.1016/j.jmmm. 2023.170587.
- [15] Lund LA, Yashkun U, Shah NA. Multiple solutions of unsteady Darcy–Forchheimer porous medium flow of Cu–Al<sub>2</sub>O<sub>3</sub>/water-based hybrid nanofluid with joule heating and viscous dissipation effect. J Therm Anal Calorim. 2024;149(5):2303–15.
- [16] Ouyang Y, Basir MFM, Naganthran K, Pop I. Unsteady magnetohydrodynamic tri-hybrid nanofluid flow past a moving wedge with viscous dissipation and Joule heating. Phys Fluids. 2024;36(6):062009. doi: 10.1063/5.0208608.
- [17] Suresh Kumar Y, Hussain S, Raghunath K, Ali F, Guedri K, Eldin SM, et al. Numerical analysis of magnetohydrodynamics Casson nanofluid flow with activation energy, Hall current and thermal radiation. Sci Rep. 2023;13(1):4021. doi: 10.1038/s41598-023-28379-5.
- [18] Sarkar A, Mondal H, Nandkeolyar R. Effect of thermal radiation and nth order chemical reaction on non-Darcian mixed convective MHD nanofluid flow with non-uniform heat source/sink. Int J Ambient Energy. 2023;44(1):1931–47.
- [19] Alharbi KAM, Farooq U, Waqas H, Imran M, Nooreen S, Akgul A, et al. Numerical solution of Maxwell-Sutterby nanofluid flow inside a stretching sheet with thermal radiation, exponential heat source/sink, and bioconvection. Int J Thermofluids. 2023;18:100339. doi: 10.1016/j.ijft.2023.100339.
- [20] Swain K, Ibrahim SM, Dharmaiah G, Noeiaghdam S. Numerical study of nanoparticles aggregation on radiative 3D flow of maxwell fluid over a permeable stretching surface with thermal radiation and heat source/sink. Res Eng. 2023;19:101208. doi: 10.1016/j. rineng.2023.101208.
- [21] Prakash O, Rao PS, Sharma RP, Mishra SR. Hybrid nanofluid MHD motion towards an exponentially stretching/shrinking sheet with the effect of thermal radiation, heat source and viscous dissipation. Pramana. 2023;97(2):64. doi: 10.1007/s12043-023-02533-0.
- [22] Khan ZH, Swain K, Ibrahim SM, Khan WA, Huang Z. Transient flow and heat transfer characteristics of single-phase nanofluid past a stretching sheet under the influence of thermal radiation and heat source. Alex Eng J. 2024;108:122–34.
- [23] Khan ZH, Khan WA, Ibrahim SM, Swain K, Huang Z. Impact of multiple slips and thermal radiation on heat and mass transfer in

- MHD Maxwell hybrid nanofluid flow over porous stretching sheet. Case Stud Therm Eng. 2024;61:104906. doi: 10.1016/j.csite.2024. 104906.
- [24] Sekhar PR, Sreedhar S, Ibrahim SM, Kumar PV, Omprakash B. Numerical investigation of heat radiation on MHD viscoelastic nanofluid flow over a stretching sheet with heat source and slip conditions. Int | Interact Des Manuf. 2024;8(5):2991-3000.
- [25] Sademaki LJ, Shamshuddin MD, Salawu SO, Reddy BP. Unsteady dynamical analysis of convective hydromagnetic thermal migration of chemically reacting tiny species with dissipation and radiation in an inclined porous plate. Int J Mod Phys B. 2024;38(32):2450442. doi: 10.1142/S0217979224504423.
- [26] Sademaki LJ, Shamshuddin MD, Reddy BP, Salawu SO. Unsteady Casson hydromagnetic convective porous media flow with reacting species and heat source: Thermo-diffusion and diffusion-thermo of tiny particles. Partial Differ Equ Appl Math. 2024;11:100867. doi: 10. 1016/j.padiff.2024.100867.
- [27] Reddy BP, Shamshuddin MD, Salawu SO, Sademaki LJ. Computational analysis of transient thermal diffusion and propagation of chemically reactive magneto-nanofluid, Brinkmantype flow past an oscillating absorbent plate. Partial Differ Equ Appl Math. 2024;11:100761. doi: 10.1016/j.padiff.2024.100761.
- Shamshuddin MD, Gamar F, Ram MS, Salawu SO. Numerical Γ281 treatment of MHD micropolar nanofluid flow with activation energy, thermal radiation, and Hall current past a porous stretching sheet. Int J Mod Simult. 2024;1-13. doi: 10.1080/ 02286203.2024.2378764.
- [29] Shamshuddin MD, Asogwa KK, Ferdows M. Thermo-solutal migrating heat producing and radiative Casson nanofluid flow via bidirectional stretching surface in the presence of bilateral reactions. Numer Heat Transf Part A: Applic. 2024;85(5):719-38.
- [30] Patil AB, Patil VS, Humane PP, Shamshuddin MD, Rajput GR. MHDdriven chemically active and thermally radiative Prandtl hybrid nanofluid flow on stretching device with Ohmic heating, dissipation, and diffusion effects. Numer Heat Transf Part A: Appl. 2024;85(13):2165-82.
- [31] Hussain SM, Mishra MR, Seth GS, Chamkha AJ. Dynamics of heat absorbing and radiative hydromagnetic nanofluids through a stretching surface with chemical reaction and viscous dissipation. Proc Instit Mech Eng Part E: J Proc Mech Eng. 2024;238(1):101–11.
- [32] Khan SA, Hayat T, Alsaedi A. Chemically reactive flow beyond constant thermophysical characteristics. Case Stud Therm Eng. 2024;61:104980. doi: 10.1016/j.csite.2024.104980.
- [33] Shamshuddin MD, Ram MS, Ashok N, Salawu SO. Exploring thermal and solutal features in stagnation point flow of Casson fluid over an exponentially radiative and reactive vertical sheet. Numer Heat Transf Part B: Fund. 2024;86(9):1-16. doi: 10.1080/10407790.2024.2355561.
- Ibrahim SM, Lorenzini G, Kumar PV, Raju CSK. Influence of chemical reaction and heat source on dissipative MHD mixed convection

- flow of a Casson nanofluid over a nonlinear permeable stretching sheet. Int J Heat Mass Transf. 2017;111:346-55.
- Brewster MQ. Thermal radiative transfer and properties. New York: John Wiley & Sons; 1992.
- [36] Liao SJ. Homotopy analysis method in non-linear differential equations. Berlin, Heidelberg: Springer; 2012. doi: 10.1007/978-3-
- Nadeem S, Hag RU, Akbar NS. MHD three-dimensional boundary layer flow of Casson nanofluid past a linearly stretching sheet with convective boundary condition. IEEE Trans Nanotechnol. 2013;13(1):109-15.
- [38] Mishra SR, Baag S, PK, Pattnaik PK, Panda S. Sensitivity analysis on enhanced thermal transport in Eyring-Powell nanofluid flow: investigating over a radiating convective Riga plate with nonuniform heat source/sink under flux conditions. I Therm Anal Calorim. 2024;149(2):711-28.
- [39] Pattnaik PK, Mishra SR, Panda S. Response surface methodology on optimizing heat transfer rate for the free convection of microstructured fluid through permeable shrinking surface. Euro Phys J Plus. 2024;139(3):221. doi: 10.1140/epjp/s13360-024-05001-9.
- [40] Ontela S, Pattnaik PK, Panda S, Mishra SR. Optimizing heat transfer rate and sensitivity analysis of hybrid nanofluid flow over a radiating sheet: Applications in solar-powered charging stations. Numer Heat Transf Part B: Fund. 2024;1-21. doi: 10.1080/10407790. 2024.2341439.
- Faroog U, Imran M, Fatima N, Noreen S, Alhushaybari A, Akgül A, [41] et al. Analysis of Kerosene oil conveying silver and manganese zinc ferrite nanoparticles with hybrid nanofluid: effects of increasing the Lorentz force, suction, and volume fraction. Ain Shams Eng J. 2024;15(1):102326. doi: 10.1016/j.asej.2023.102326.
- [42] Waqas H, Farooq U, Hassan A, Liu D, Noreen S, Makki R, et al. Numerical and Computational simulation of blood flow on hybrid nanofluid with heat transfer through a stenotic artery: Silver and gold nanoparticles. Res Phys. 2023;44:106152. doi: 10.1016/j.rinp. 2022.106152.
- [43] Alqawasmi K, Alharbi KAM, Farooq U, Noreen S, Imran M, Akgül A, et al. Numerical approach toward ternary hybrid nanofluid flow with nonlinear heat source-sink and Fourier heat flux model passing through a disk. Int | Thermofluids. 2023;18:100367. doi: 10. 1016/j.ijft.2023.100367.
- [44] Mishra A. Analysis of waste discharge concentration in radiative hybrid nanofluid flow over a stretching/shrinking sheet with chemical reaction. Mech Time-Depend Mat. 2025;29(1):7. doi: 10. 1007/s11043-024-09752-x.
- [45] Mishra A, Rawat SK, Yaseen M, Pant M. Development of machine learning algorithm for assessment of heat transfer of ternary hybrid nanofluid flow towards three different geometries: Case of artificial neural network. Heliyon. 2023;9(11):e21453. doi: 10.1016/j. heliyon.2023.e21453.